

**First Results from the Taiwan Axion Search Experiment with
Haloscope at $20\,\mu\text{eV}/c^2$ ***

Ann Author[†] and Second Author[‡]

Authors' institution and/or address

*This line break forced with *

(TASEH Collaboration)

(Dated: January 10, 2022)

Abstract

This paper presents the first results from the Taiwan Axion Search Experiment with Haloscope, a search for axions using a microwave cavity at frequencies between 4.707506 and 4.798145 GHz. Apart from external signals, no candidates with significance more than 3.355σ were found. The experiment excludes models with the axion-two-photon coupling $g_{a\gamma\gamma} \gtrsim zzzz \times 10^{-13} \text{ GeV}^{-1}$, a factor of ten above the benchmark KSVZ model for the mass range $xxxx < m_a < yyyy \mu\text{eV}/c^2$. For the first time, constraints on the $g_{a\gamma\gamma}$ have been placed in this mass region.

CONTENTS

I. Introduction	3
A. The expected axion signal power and signal line shape	4
B. The expected noise and the signal-to-noise ratio	6
II. Experimental Setup	7
III. Analysis Procedure	9
A. Analysis overview	9
B. Fast Fourier transform	9
C. Gain	10
D. Remove the oscillating structure	10
E. Combine spectra with weighting algorithm	11
F. Merging bins	12
IV. Analysis of the synthetic axions data	13
V. Systematic Uncertainties	13
VI. Results	14
VII. Conclusion	14

* A footnote to the article title

† Also at Physics Department, XYZ University.

‡ Second.Author@institution.edu

31	Acknowledgments	14
32	A. The derivation of the noise spectrum from the cavity	14
33	References	16

34 I. INTRODUCTION

35 The axion is a hypothetical particle predicted as a consequence of a solution to the
36 strong CP problem [1–3], i.e. why the product of the charge conjugation (C) and parity (P)
37 symmetries is preserved in the strong interactions when there is an explicit CP-violating term
38 in the QCD Lagrangian. In other words, why is the electric dipole moment of the neutron
39 so tiny: $|d_n| < 1.8 \times 10^{-26} e \cdot \text{cm}$ [4, 5]? The solution proposed by Peccei and Quinn is to
40 introduce a new global Peccei-Quinn $U(1)_{\text{PQ}}$ symmetry that is spontaneously broken; the
41 axion is the pseudo Nambu-Goldstone boson of $U(1)_{\text{PQ}}$ [1]. Axions are abundantly produced
42 during the QCD phase transition in the early universe and may constitute the dark matter
43 (DM). In the post-inflationary PQ symmetry breaking scenario, where the PQ symmetry
44 is broken after inflation, current calculations suggest a mass range of 1–100 $\mu\text{eV}/c^2$ for
45 axions so that the cosmic axion density does not exceed the observed cold DM density [6–
46 18]. Refs [19–21] also suggested that axions form a Bose-Einstein condensate; this property
47 explains the occurrence of caustic rings in galactic halos. Therefore, axions are compelling
48 because they may explain at the same time puzzles that are on scales different by more than
49 thirty orders of magnitude.

50 Axions could be detected and studied via their two-photon interaction, the so-called
51 “inverse Primakoff effect”. For QCD axions, i.e. the axions proposed to solve the strong CP
52 problem, the axion-two-photon coupling constant $g_{a\gamma\gamma}$ is related to the mass of the axion
53 m_a :

$$54 \quad g_{a\gamma\gamma} = \left(\frac{g_\gamma \alpha}{\pi \Lambda^2} \right) m_a, \quad (1)$$

55 where g_γ is a dimensionless model-dependent parameter, α is the fine-structure constant,
56 $\Lambda = 78 \text{ MeV}$ is a scale parameter that can be derived from the mass and the decay constant
57 of the pion, and the ratio of the up to down quark masses. The numerical values of g_γ
58 are -0.97 and 0.36 in the Kim-Shifman-Vainshtein-Zakharov (KSVZ) [22, 23] and the Dine-
59 Fischler-Srednicki-Zhitnitsky (DFSZ) [24, 25] benchmark models, respectively.

The detectors with the best sensitivities to axions with a mass of $\approx \mu\text{eV}/c^2$, as first put forward by Sikivie [26, 27], are haloscopes consisting of a microwave cavity immersed in a strong static magnetic field and operated at a temperature below 0.1 K. In the presence of an external magnetic field, the ambient oscillating axion field induces an electric current that oscillates with a frequency ν set by the total energy of the axion: $h\nu = E_a = m_a c^2 + \frac{1}{2}m_a v^2$. The induced electric current and the microwave cavity act as coupled oscillators and resonate when the frequencies of the electromagnetic modes in the cavity match ν ; the signal power is further delivered in the form of microwave photons and readout with a low-noise amplifier. The axion mass is unknown, therefore, the cavity resonator must allow the possibility to be tuned through a range of possible axion masses. Over the years, the Axion Dark Matter eXperiment (ADMX) had developed and improved the cavity design and readout electronics and excluded KSVZ benchmark model within the mass range of 1.9–4.2 $\mu\text{eV}/c^2$ and DFSZ benchmark model for the mass range of 2.66–3.31 $\mu\text{eV}/c^2$ [28–34]. The Haloscope at Yale Sensitive to Axion Cold dark matter (HAYSTAC) [35] and the Center for Axion and Precision Physics Research (CAPP) [36] aim for axions at higher masses and have pushed the limits on $g_{a\gamma\gamma}$ towards the KSVZ value for the mass ranges of 16.96–17.12 and 17.14–17.28 $\mu\text{eV}/c^2$, and 10.7126–10.7186 $\mu\text{eV}/c^2$, respectively. This paper presents the first results and the analysis details of a search for axions for the mass range of $xxxx\text{--}yyyy \mu\text{eV}/c^2$, from the Taiwan Axion Search Experiment with Haloscope (TASEH).

A. The expected axion signal power and signal line shape

The signal power extracted from a microwave cavity on resonance is given by:

$$P_s = \left(g_\gamma^2 \frac{\alpha^2 \hbar^3 c^3 \rho_a}{\pi^2 \Lambda^4} \right) \times \left(\omega_c \frac{1}{\mu_0} B_0^2 V C_{mnl} Q_L \frac{\beta}{1 + \beta} \right), \quad (2)$$

where $\rho_a = 0.45 \text{ GeV}/\text{cm}^3$ is the local dark-matter density. The second set of parentheses contains parameters related to the experimental setup: the angular resonance frequency of the cavity ω_c , the vacuum permeability μ_0 , the average strength of the external magnetic field B_0 , the volume of the cavity V , and the loaded quality factor of the cavity $Q_L = Q_0/(1 + \beta)$, where Q_0 is the unloaded, intrinsic quality factor of the cavity and β determines the amount of coupling of the signal to the receiver. The form factor C_{mnl} is the normalized overlap of the electric field $\vec{\mathbf{E}}$, for a particular cavity resonant mode, with the external magnetic field

\vec{B} :

$$C_{mnl} = \frac{\left[\int (\vec{B} \cdot \vec{E}_{mnl}) d^3\mathbf{x} \right]^2}{B_0^2 V \int E_{mnl}^2 d^3\mathbf{x}}. \quad (3)$$

Here, the magnetic field \vec{B} points mostly along the axial direction (z -axis) of the cavity. The field strength has a small variation along the radial and axial directions and B_0 is the averaged value over the whole cavity volume. For cylindrical cavities, the largest form factor is from the TM_{010} mode. The expected signal power derived from the experimental parameters of TASEH (see Table I) is $P_s \simeq 1.5 \times 10^{-24}$ W for a KSVZ axion with a mass of $19.5 \mu\text{eV}/c^2$.

In most of the direct dark matter search experiments, several assumptions were made in order to derive a signal line shape. The density and the velocity distributions of DM are related to each other through the gravitational potential. The DM in the galactic halo is assumed to be virialized. The DM halo density distribution is assumed to be spherically symmetric and close to be isothermal, which results in a velocity distribution similar to the Maxwell-Boltzmann distribution. The distribution of the measured signal frequency can be further derived from the velocity distribution after a change of variables and set $h\nu_a = m_a c^2$. Previous experimental results typically adopt the following function for frequency $\nu \geq \nu_a$:

$$f(\nu) = \frac{2}{\sqrt{\pi}} \sqrt{\nu - \nu_a} \left(\frac{3}{\alpha} \right)^{3/2} e^{\frac{-3(\nu - \nu_a)}{\alpha}}, \quad (4)$$

where $\alpha \equiv \nu_a \langle v^2 \rangle / c^2$ and is related to the variance of the velocity distribution. For the Maxwell-Boltzmann distribution, $\langle v^2 \rangle = 3v_c^2/2 = (270 \text{ km/s})^2$ where $v_c = 220 \text{ km/s}$ is the local circular velocity of DM in the galactic rest frame. Equation (4) is modified if one considers that the relative velocity of the DM halo with respect to the Earth is not the same as the DM velocity in the galactic rest frame [37]. The velocity distributions shall also be truncated so that the DM velocity is not larger than the escape velocity of the Milky Way [38]. Several N-body simulations [39, 40] follow structure formation from the initial DM density perturbations to the largest halo today and take into account the merger history of the Milky Way, rather than assuming that the Milky Way is in a steady state; the simulated results suggest velocity distributions with more high-speed particles relative to the Maxwellian case [41, 42]. However, these numerical simulations contain only DM particles; an inclusion of baryons may enhance the halo's central density due to a condensation of gas towards the center of the halo via an adiabatic contraction [43, 44], or may reduce the

density due to the supernova outflows, etc [45, 46].

In order to compare the results of TASEH with those of the former experiments, the analysis presented in this paper assumes an axion signal line shape by including Eq. (4) in the weights when merging the measured power from multiple frequency bins (see Section III). Nevertheless, given the caveats above and a lack of strong evidence for any particular choice of velocity distributions, the results without an assumption of signal line shape and the results with a simple Gaussian weight are also presented for comparison. In addition, a signal line width $\Delta\nu_a = m_a \langle v^2 \rangle / h \simeq 5$ kHz, which is much smaller than the TASEH cavity line-width $\nu_a/Q_L \simeq 250$ kHz, is assumed and five frequency bins are merged to perform the final analysis.

B. The expected noise and the signal-to-noise ratio

Several physics processes can contribute to the total noise and all of them can be seen as Johnson thermal noise at some effective temperature, or the so-called system noise temperature T_{sys} . The total noise power in a bandwidth $\Delta\nu$ is then:

$$P_n = k_B T_{\text{sys}} \Delta\nu, \quad (5)$$

where k_B is the Boltzmann constant. The system noise temperature T_{sys} has three major components:

$$k_B T_{\text{sys}} = h\nu \left(\frac{1}{e^{h\nu/k_B T_{\text{cavity}}} - 1} + \frac{1}{2} + N_A \right). \quad (6)$$

The three terms in Eq. (6) correspond to the blackbody radiation from the cavity at temperature T_{cavity} , the quantum noise associated with the zero-point fluctuation of the blackbody gas, and the noise added by the receiver N_A . The first term in Eq. (6) implies that the noise spectrum from the cavity has little dependence on the frequency (white spectrum) for the narrow bandwidth considered in the experiment. However, the noise spectrum observed by TASEH was actually Lorentzian due to the temperature difference between the cavity and the transmission line in the dilution refrigerator. More details may be found in Section II and Appendix A.

Using the operation parameters of TASEH in Table I, the effective temperatures of these three sources are estimated to be about 0.07 K, 0.11 K, and 2.1 K, respectively. Therefore, the value of T_{sys} for TASEH is about 2.3 K, which gives a noise power of approximately

1.6 $\times 10^{-19}$ W for a bandwidth of 5 kHz (the assumed axion signal line-width), three orders of magnitude larger than the signal. Nevertheless, what matters in the analysis is the signal significance, or the so-called signal-to-noise ratio (SNR) using the standard terminology of axion experiments, i.e. the ratio of the signal power to the uncertainty in the estimate of the noise power:

$$\begin{aligned} \text{SNR} &= \frac{P_s}{\delta P_n} = \frac{P_s}{P_n} \sqrt{\Delta\nu_a \tau}, \\ &= \frac{P_s}{k_B T_{\text{sys}}} \sqrt{\frac{\tau}{\Delta\nu_a}}, \end{aligned} \quad (7)$$

where τ is the amount of data integration time. Equation (7) can be derived from Dicke's Radiometer Equation, assuming that the amplitude distribution of the noise voltage within a bandwidth $\Delta\nu_a$ is Gaussian.

II. EXPERIMENTAL SETUP

The detector of TASEH is located at the Department of Physics, National Central University, Taiwan and housed within a cryogen-free dilution refrigerator (DR) from BlueFors. A 8-Tesla superconducting solenoid with a bore diameter of 76 mm and a length of 240 mm is integrated with the DR.

During the data taking, the cavity sat in the center of the magnet bore and was connected via holders to the mixing chamber plate of the DR at a temperature of ≈ 30 mK. Due to an inefficiency of thermal conduction and thermal radiation, the temperature of the cavity stayed at 155 mK, higher with respect to the DR. The cavity, made of oxygen-free high-conductivity (OFHC) copper, has an effective volume of 0.234 L and is a two-cell cylinder split along the axial direction (z -axis). The cylindrical cavity has an inner radius of 2.5 cm and a height of 12 cm. In order to maintain a smooth surface, the cavity underwent the processes of polishing, chemical cleaning, and annealing. The resonance frequency of the TM_{010} mode can be tuned over the range of 4.717–4.999 GHz via the rotation of an off-axis OFHC copper tuning rod, from the position closer to the cavity wall to the position closer to the cavity center. The form factor C_{010} as defined in Eq. (3) varies from 0.64 to 0.69 over the full frequency range. The intrinsic, unloaded quality factor Q_0 at the cryogenic temperature ($T_{\text{cavity}} \simeq 155$ mK) is $\simeq 60000$ at the frequency of 4.74 GHz.

TABLE I. The benchmark experimental parameters for estimating the sensitivity of TASEH. The definitions of the parameters can be found in Section I. See Sec. III and Ref. [?] for the values obtained during the data run.

f_{lo}	4.707506 GHz
f_{hi}	4.798145 GHz
B_0	8 Tesla
V	0.234 L
C_{010}	0.65
Q_0	60000
β	2
T_{cavity}	155 mK
T_{sys}	2.3 K
$\Delta\nu_a$	5 kHz
$\nu_{\text{resolution}}$	1 KHz

An output probe, made of a 50- Ω semi-rigid coaxial cable soldering SMA plug crimp, was inserted into the cavity and its depth was set for $\beta \simeq 2$. The signal from the output probe was directed to an impedance-matched amplification chain. The first-stage amplifier was a low noise high-electron-mobility transistor (HEMT) amplifier with an effective noise temperature of ≈ 2 K, mounted on the 4K-flange. The signal was further amplified at room temperature and down-converted and demodulated to in-phase (I) and quadrature (Q) components and digitized by an analog-to-digital converter (ADC) with a sampling rate of 2 MHz. The frequency resolution of the spectra was 1 kHz.

A more detailed description of the TASEH detector, the operation of the data run, and the calibration of the gain and added noise temperature of HEMT can be found in Ref. [?]. See Table I for the benchmark experimental parameters that can be used to estimate the sensitivity of TASEH.

III. ANALYSIS PROCEDURE

A. Analysis overview

Our goal is to find the axion signal hidden in the white noise. In order to achieve this, our analysis procedure includes the following steps:

1. Perform Fast Fourier transform (FFT) time-dependent spectrum to obtain the frequency-dependent spectrum.
2. Divide the measured power by the gains from the receiver chain to retrieve real power from cavity.
3. Use the results of high-electron-mobility-transistor (HEMT) drifting (see Section ??) to predict adding noise and gain; the input environmental parameters include monitoring temperatures, voltages of power supplies, etc.
4. Apply Savitzky-Golay (SG) filter to the oscillating structure of the frequency-dependent spectrum
5. Combine all power spectra from different frequency scans with weighting algorithm.
6. Merge bins in the combined spectrum to maximize the signal-to-noise ratio (SNR).
7. Set limit on $g_{a\gamma\gamma}$.

B. Fast Fourier transform

For each frequency scan, we collected data for 12.5 hours. The recorded data were stored in TDMS files (Technical Data Management Streaming - binary file format developed by **National Instruments**). Each TDMS file contains 2 millions data points corresponding to 1000 time dependent subspectra. We performed Fast Fourier Transform (FFT) on each subspectrum to get the power in frequency (Eq.8). The I and Q in Eq.8 are the raw data in voltage, R (50 Ohms) is the resistor of the signal analyzer, and 2000 is the number of data points. Finally, we averaged every 1000 successive subspectra to obtain the mean power in one second.

$$\text{Power} = \frac{|\text{FFT}(I + i \cdot Q)|^2}{2000 \cdot 2R} \quad (8)$$

C. Gain

The net gain of our receiver chain includes: down conversion gain, Intermediate Frequency(IF) attenuator, Radio Frequency(RF) attenuator and HEMT gain. The first three were the parameters set during data taking, the last one was estimated from calibration (Section ??). Fig.1 shows the gain and noise from the HEMT calibration done before the data run.

After removing all the gains, we got the real power going out from the antenna of the cavity. The variation of the real power in time is shown in Fig. 2. One possible cause of this effect came from the additional gain variation that was not studied in the initial HEMT calibration before taking data. To investigate this issue, we did HEMT drifting to check the behaviour of the gain over time.

FIG. 1. Gain and noise of HEMT before running data

FIG. 2. Power over the time from step 1 to step 16

D. Remove the oscillating structure

Figure ?? illustrates one raw output power at the receiver chain. The non-flat power spectrum is caused by the product of the system noise and the net gain. We remove the structure by using the Savitzky Golay (SG) filter [?]. The SG filter is a digital filter that can smooth data without distorting the signal tendency. This is done by fitting adjacent points of successive sub-sets of data with a polynomial of order n . The result depends on two parameters which are the number of data points used in the fitting, so-called window width, and order of the polynomial. If the window is too wide, the filter will not remove small structures whereas if it is too narrow, it may kill the signal. The window was chosen

FIG. 3. (a) The power spectra after average 12.5 hours of data. (b) Raw power of 1s data (blue line) and the output Savitzky-Golay filter (red line). (c) After dividing the sg filter's result in every step (d) The system temperature derived from μ and σ .

based on the system noise temperature calculated from the mean (μ) and standard deviation (σ) of the output power.

$$\mu = k_B \cdot T_S \cdot \Delta\nu \quad (9)$$

$$\sigma = \frac{k_B \cdot T_S \cdot \Delta\nu}{\sqrt{N}} \quad (10)$$

where k_B is the Boltzmann constant, T_S is the system temperature, $\Delta\nu$ is the frequency resolution and N is the number of averaging.

If the chosen window is appropriate, the system temperature estimated from μ and σ should be consistent with each other.

We also did some studies to check if the SG filter removed the axion signal. Assuming a signal bandwidth of 5 kHz, we added the signal into noise spectrum and applied the SG filter. The result shows that the filter does not suppress the axion signal as given in Fig.5.

The normalized spectrum was obtained by dividing the raw spectrum by the baseline - output of the SG filter - and subtract 1. Therefore, if the signal exists, the excess power will be above 0.

FIG. 4. The simulation for testing the effect of SG filter.

FIG. 5. Weighed SNR

E. Combine spectra with weighting algorithm

The purpose of weighting algorithm is to add different spectra in Fig. ?? vertically, particularly for the frequency bins that appear in multiple spectra. Each spectrum in Fig.?? was collected with a different cavity resonance frequency. Therefore, if a signal appears in a certain frequency bin n^{th} , due to the difference in resonance frequency and Lorentzian height, the expected signal power will be different in each spectrum i . The weighting algorithm is expected to take this into account.

$$w_n^i = \frac{h \cdot p}{(\sigma_n^i)^2} \quad (11)$$

We have a weight Eq.(11), where w_n^i means the weight in the n^{th} bin of the i^{th} spectrum, and h follows the line shape of the cavity which is a Lorentz' distribution; the value of h

will be larger when the frequency bin is closer to the cavity resonance frequency , p is the expected axion power.

$$(\delta_{weighted})_n = \frac{\sum_i^k \delta_n^i \cdot w_n^i}{\sum_i^k w_n^i} \quad (12)$$

$$(\sigma_{weighted})_n = \frac{\sqrt{\sum_i^k (\sigma_n^i \cdot w_n^i)^2}}{\sum_i^k w_n^i} \quad (13)$$

$$(SNR_{weighted})_n = \frac{(\delta_{weighted})_n}{(\sigma_{weighted})_n} = \frac{\sum_i^k \delta_n^i \cdot w_n^i}{\sqrt{\sum_i^k (\sigma_n^i \cdot w_n^i)^2}} \quad (14)$$

where δ_n^i and σ_n^i are the measured power and the corresponding standard deviation of the n^{th} frequency bin of the i^{th} spectrum., From the weighted power in n^{th} bin in Eq.(12), and weighted σ in Eq.(13), we can get our Signal to noise ratio as Eq.(14)

F. Merging bins

In theory, the expected Axion bandwidth is 5KHz, and our frequency resolution is 1KHz, therefore we need to merge 5 bins. Due to the expected Maxwellian signal line shape, a weight will be applied when merging five neighbouring bins

$$w_q = \frac{L_q}{(weighted \sigma_q)^2} \quad (15)$$

$$f(\nu) = \frac{2}{\sqrt{\pi}} \sqrt{\nu - \nu_a} \left(\frac{3}{\nu_a \langle \beta^2 \rangle} \right)^{\frac{3}{2}} e^{-\frac{3(\nu - \nu_a)}{\nu_a \langle \beta^2 \rangle}} \quad (16)$$

$$L_q = \int_{\nu_a + \nu_q + (q+1)\Delta\nu}^{\nu_a + \nu_q + q\Delta\nu} f(\nu) d\nu \quad (17)$$

We have a weight Eq.(15), where L_q is the area in q^{th} bin and σ_q is the weighted σ in the q^{th} bin , Eq.(16) is the axion CDM(cold dark matter) line shape, where $\langle \beta^2 \rangle = \langle v^2 \rangle / c^2$ and $\langle v^2 \rangle = (270 \text{ km/s})^2$, $\langle v^2 \rangle$ is the squared virial velocity. Eq.(17),

$$(\delta_{merged})_q = k \cdot \frac{\sum_{i=q-k/2}^{q+k/2} (\delta_{weighted})_q^i \cdot w_q}{\sum_{i=q-k/2}^{q+k/2} w_q} \quad (18)$$

$$(\sigma_{merged})_q = k \cdot \frac{\sqrt{\sum_{i=q-k/2}^{q+k/2} (\sigma_{weighted})_q^i \cdot w_q}}{\sum_{i=q-k/2}^{q+k/2} w_q^2} \quad (19)$$

$$(SNR_{merged})_q = \frac{(\delta_{merged})_q}{(\sigma_{merged})_q} = \frac{\sum_{i=q-k/2}^{q+k/2} (\delta_{weighted})_q^i \cdot w_q}{\sqrt{\sum_{i=q-k/2}^{q+k/2} (\sigma_{weighted})_q^i \cdot w_q}} \quad (20)$$

Adding adjacent bin with a weight Eq.(18) Eq.(19), where k is the number of adjacent bin to be merged, q is q^{th} merged bin, with Eq.(19), we can get our weighted merged power spectrum FIG.6.

FIG. 6. The merged power δ following Eq.(18), standard deviation σ derived from Eq.(19), and signal to noise ratio SNR from Eq.(19)

FIG. 7. Our SNR target is 5σ , so if we want to have 95% of confidence, the threshold need to be 3.355σ ($5\sigma - 1.645\sigma$).

IV. ANALYSIS OF THE SYNTHETIC AXIONS DATA

V. SYSTEMATIC UNCERTAINTIES

In order to understand the systematic errors, We reviewed the steps of the analysis and listed the possible causes of systematic errors.

First is the SG filter, using different window and order will give us slightly different result, so we will try different SG filter and count them as systematic error.

Second is the gain, we don't understand much about Hemt gain now, so we use the calibrated gain before the data taking as our systematic error.

Third, when doing the weighting algorithm Section. III E, σ is included in the weight. In theory, the system temperature derived from σ and μ should be the same, But in Fig??, they are not exactly the same, Therefore, a systematic uncertainty is derived by replacing σ with $\frac{\mu}{\sqrt{N}}$, where N is the number of spectra that share the same frequency bin.

I will sum Up these limit with following formula.

$$\text{error band} = \sqrt{(G_{\gamma 1} - G_{\gamma 0})^2 + (G_{\gamma 2} - G_{\gamma 0})^2 + \dots}$$

FIG. 8. using different window and order to test the sg filter, With order 3 window 101, we have the largest σ , It seems that low order and high windows have some problems.

FIG. 9. step 1 after sg filter, It seems like low order and high filter can't remove the periodic structure well.

FIG. 10. Using the Original and predict Gain gives us similar result.

FIG. 11. In principle, the system temperature calculate by σ and μ should be the same, so I replace the

FIG. 12. After sum all the limit to get the systematic error band

VI. RESULTS

In Fig.7, we set a threshold at 3.355σ , if the expected signal is 5σ above the noise level, the signal is supposed to have 95% of the chance passing the cut at 3.355 sigma. However, a signal was not observed. Therefore, with 95% C.L., the signal cannot be larger than 5σ .

FIG. 13. Set the limit with 5σ

VII. CONCLUSION

ACKNOWLEDGMENTS

Appendix A: The derivation of the noise spectrum from the cavity

The Hamiltonian of a single-mode cavity is

$$H = \hbar\omega_c(C^\dagger C + \frac{1}{2}), \quad (\text{A1})$$

where $\omega_c/2\pi$ is the cavity resonance frequency and C is the annihilation operator of the inner cavity field. The cavity field is coupled to the modes A of a transmission line with the rate κ_2 . The cavity field is also coupled to the environment modes B with the rate κ_0 . Based on the model of Fig. 14 and the input-output theory, the equation of motion for C is

obtained:

$$\frac{dC}{dt} = -i\omega_c C - \frac{\kappa_2 + \kappa_0}{2} C + \sqrt{\kappa_2} A_{\text{in}} + \sqrt{\kappa_0} B_{\text{in}}. \quad (\text{A2})$$

A boundary condition holds for the transmission modes:

$$A_{\text{out}} = \sqrt{\kappa_2} C - A_{\text{in}}. \quad (\text{A3})$$

Considering working in a rotating frame of the signal frequency ω near ω_c , the equation of motion becomes:

$$-i\omega C + \frac{dC}{dt} = -i\omega_c C - \frac{\kappa_2 + \kappa_0}{2} C + \sqrt{\kappa_2} A_{\text{in}} + \sqrt{\kappa_0} B_{\text{in}}. \quad (\text{A4})$$

The steady state solution for the cavity field is:

$$C = \frac{\sqrt{\kappa_2} A_{\text{in}} + \sqrt{\kappa_0} B_{\text{in}}}{-i(\omega - \omega_c) + \frac{\kappa_2 + \kappa_0}{2}}. \quad (\text{A5})$$

By substituting Eq. (A5) into Eq. (A3), the reflected modes of the transmission line A_{out} are expressed in terms of the input modes of the transmission line A_{in} and the environment B_{in} :

$$\begin{aligned} A_{\text{out}} &= \frac{i(\omega - \omega_c) + \frac{\kappa_2 - \kappa_0}{2}}{-i(\omega - \omega_c) + \frac{\kappa_2 + \kappa_0}{2}} A_{\text{in}} + \frac{\sqrt{\kappa_2 \kappa_0}}{-i(\omega - \omega_c) + \frac{\kappa_2 + \kappa_0}{2}} B_{\text{in}} \\ &= \frac{-(\omega - \omega_c)^2 + \frac{\kappa_2^2 - \kappa_0^2}{4} + i\kappa_2(\omega - \omega_c)}{(\omega - \omega_c)^2 + (\frac{\kappa_2 + \kappa_0}{2})^2} A_{\text{in}} + \frac{\sqrt{\kappa_2 \kappa_0} \frac{\kappa_2 + \kappa_0}{2} + i\sqrt{\kappa_2 \kappa_0}(\omega - \omega_c)}{(\omega - \omega_c)^2 + (\frac{\kappa_2 + \kappa_0}{2})^2} B_{\text{in}}. \end{aligned} \quad (\text{A6})$$

Therefore, the autocorrelation of A_{out} is related to those of A_{in} and B_{in} :

$$\begin{aligned} \langle A_{\text{out}}^\dagger A_{\text{out}} \rangle &= \frac{[(\omega - \omega_c)^2 - \frac{\kappa_2^2 - \kappa_0^2}{4}]^2 + \kappa_2^2(\omega - \omega_c)^2}{[(\omega - \omega_c)^2 + (\frac{\kappa_2 + \kappa_0}{2})^2]^2} \langle A_{\text{in}}^\dagger A_{\text{in}} \rangle \\ &\quad + \frac{\kappa_2 \kappa_0 (\frac{\kappa_2 + \kappa_0}{2})^2 + \kappa_2 \kappa_0 (\omega - \omega_c)^2}{[(\omega - \omega_c)^2 + (\frac{\kappa_2 + \kappa_0}{2})^2]^2} \langle B_{\text{in}}^\dagger B_{\text{in}} \rangle. \end{aligned} \quad (\text{A7})$$

The spectrum from the cavity $S(\omega)$ is found to be related to the spectrum of the readout transmission line $S_{\text{rt}}(\omega)$ and the spectrum of the cavity environment $S_{\text{cav}}(\omega)$:

$$\begin{aligned} S(\omega) &= \frac{[(\omega - \omega_c)^2 - \frac{\kappa_2^2 - \kappa_0^2}{4}]^2 + \kappa_2^2(\omega - \omega_c)^2}{[(\omega - \omega_c)^2 + (\frac{\kappa_2 + \kappa_0}{2})^2]^2} S_{\text{rt}}(\omega) \\ &\quad + \frac{\kappa_2 \kappa_0 (\frac{\kappa_2 + \kappa_0}{2})^2 + \kappa_2 \kappa_0 (\omega - \omega_c)^2}{[(\omega - \omega_c)^2 + (\frac{\kappa_2 + \kappa_0}{2})^2]^2} S_{\text{cav}}(\omega). \end{aligned} \quad (\text{A8})$$

As the the readout transmission line and the cavity environment are both in thermal states, i.e. $S_{\text{rt}}(\omega) = [n_{\text{BE}}(T_{\text{rt}}) + 1/2] \hbar\omega$ and $S_{\text{cav}}(\omega) = [n_{\text{BE}}(T_{\text{cav}}) + 1/2] \hbar\omega$, where n_{BE} is the mean




fig:cavity_in_out.jpg

FIG. 14. A cavity is coupled to the modes of transmission line A with the rate κ_2 and the modes of environment B with the rate κ_0 .

photon number given by the Bose-Einstein distribution, $S(\omega)$ is white if $T_{\text{cav}} = T_{\text{rt}}$, and Lorentzian if $T_{\text{cav}} \gg T_{\text{rt}}$.

-
- [1] R. D. Peccei and H. R. Quinn, CP conservation in the presence of pseudoparticles, Phys. Rev. Lett. **38**, 1440 (1977).
 - [2] S. Weinberg, A new light boson?, Phys. Rev. Lett. **40**, 223 (1978).
 - [3] F. Wilczek, Problem of strong p and t invariance in the presence of instantons, Phys. Rev. Lett. **40**, 279 (1978).
 - [4] C. Abel *et al.* (nEDM), Measurement of the permanent electric dipole moment of the neutron, Phys. Rev. Lett. **124**, 081803 (2020), arXiv:2001.11966 [hep-ex].
 - [5] P. D. Group, P. A. Zyla, R. M. Barnett, J. Beringer, O. Dahl, D. A. Dwyer, D. E. Groom, C. J. Lin, K. S. Lugovsky, E. Pianori, D. J. Robinson, C. G. Wohl, W. M. Yao, K. Agashe, G. Aielli, B. C. Allanach, C. Amsler, M. Antonelli, E. C. Aschenauer, D. M. Asner, H. Baer, S. Banerjee, L. Baudis, C. W. Bauer, J. J. Beatty, V. I. Belousov, S. Bethke, A. Bettini, O. Biebel, K. M. Black, E. Blucher, O. Buchmuller, V. Burkert, M. A. Bychkov, R. N. Cahn, M. Carena, A. Cecucci, A. Cerri, D. Chakraborty, R. S. Chivukula, G. Cowan, G. D'Ambrosio, T. Damour,

D. de Florian, A. de Gouvêa, T. DeGrand, P. de Jong, G. Dissertori, B. A. Dobrescu,
 M. D’Onofrio, M. Doser, M. Drees, H. K. Dreiner, P. Eerola, U. Egede, S. Eidelman, J. Ellis,
 J. Erler, V. V. Ezhela, W. Fetscher, B. D. Fields, B. Foster, A. Freitas, H. Gallagher, L. Gar-
 ren, H. J. Gerber, G. Gerbier, T. Gershon, Y. Gershtein, T. Gherghetta, A. A. Godizov, M. C.
 Gonzalez-Garcia, M. Goodman, C. Grab, A. V. Gritsan, C. Grojean, M. Grünewald, A. Gurtu,
 T. Gutsche, H. E. Haber, C. Hanhart, S. Hashimoto, Y. Hayato, A. Hebecker, S. Heinemeyer,
 B. Heltsley, J. J. Hernández-Rey, K. Hikasa, J. Hisano, A. Höcker, J. Holder, A. Holtkamp,
 J. Huston, T. Hyodo, K. F. Johnson, M. Kado, M. Karliner, U. F. Katz, M. Kenzie, V. A.
 Khoze, S. R. Klein, E. Klempt, R. V. Kowalewski, F. Krauss, M. Kreps, B. Krusche, Y. Kwon,
 O. Lahav, J. Laiho, L. P. Lellouch, J. Lesgourgues, A. R. Liddle, Z. Ligeti, C. Lippmann,
 T. M. Liss, L. Littenberg, C. Lourenço, S. B. Lugovsky, A. Lusiani, Y. Makida, F. Mal-
 toni, T. Mannel, A. V. Manohar, W. J. Marciano, A. Masoni, J. Matthews, U. G. Meißner,
 M. Mikhasenko, D. J. Miller, D. Milstead, R. E. Mitchell, K. Mönig, P. Molaro, F. Moortgat,
 M. Moskvic, K. Nakamura, M. Narain, P. Nason, S. Navas, M. Neubert, P. Nevski, Y. Nir,
 K. A. Olive, C. Patrignani, J. A. Peacock, S. T. Petcov, V. A. Petrov, A. Pich, A. Piepke,
 A. Pomarol, S. Profumo, A. Quadt, K. Rabbertz, J. Rademacker, G. Raffelt, H. Ramani,
 M. Ramsey-Musolf, B. N. Ratcliff, P. Richardson, A. Ringwald, S. Roesler, S. Rolli, A. Ro-
 maniouk, L. J. Rosenberg, J. L. Rosner, G. Rybka, M. Ryskin, R. A. Ryutin, Y. Sakai,
 G. P. Salam, S. Sarkar, F. Sauli, O. Schneider, K. Scholberg, A. J. Schwartz, J. Schwiening,
 D. Scott, V. Sharma, S. R. Sharpe, T. Shutt, M. Silari, T. Sjöstrand, P. Skands, T. Skwarnicki,
 G. F. Smoot, A. Soffer, M. S. Sozzi, S. Spanier, C. Spiering, A. Stahl, S. L. Stone, Y. Sum-
 ino, T. Sumiyoshi, M. J. Syphers, F. Takahashi, M. Tanabashi, J. Tanaka, M. Taševský,
 K. Terashi, J. Terning, U. Thoma, R. S. Thorne, L. Tiator, M. Titov, N. P. Tkachenko,
 D. R. Tovey, K. Trabelsi, P. Urquijo, G. Valencia, R. Van de Water, N. Varelas, G. Venan-
 zoni, L. Verde, M. G. Vinçter, P. Vogel, W. Vogelsang, A. Vogt, V. Vorobyev, S. P. Wakely,
 W. Walkowiak, C. W. Walter, D. Wands, M. O. Wascko, D. H. Weinberg, E. J. Weinberg,
 M. White, L. R. Wiencke, S. Willocq, C. L. Woody, R. L. Workman, M. Yokoyama, R. Yoshida,
 G. Zanderighi, G. P. Zeller, O. V. Zenin, R. Y. Zhu, S. L. Zhu, F. Zimmermann, J. Ander-
 son, T. Basaglia, V. S. Lugovsky, P. Schaffner, and W. Zheng, Review of Particle Physics,
 Progress of Theoretical and Experimental Physics **2020**, 10.1093/ptep/ptaa104 (2020),
 083C01, <https://academic.oup.com/ptep/article-pdf/2020/8/083C01/34673722/ptaa104.pdf>.

- [6] S. Borsanyi *et al.*, Calculation of the axion mass based on high-temperature lattice quantum chromodynamics, *Nature* **539**, 69 (2016), arXiv:1606.07494 [hep-lat].
- [7] M. Dine, P. Draper, L. Stephenson-Haskins, and D. Xu, Axions, Instantons, and the Lattice, *Phys. Rev. D* **96**, 095001 (2017), arXiv:1705.00676 [hep-ph].
- [8] T. Hiramatsu, M. Kawasaki, T. Sekiguchi, M. Yamaguchi, and J. Yokoyama, Improved estimation of radiated axions from cosmological axionic strings, *Phys. Rev. D* **83**, 123531 (2011), arXiv:1012.5502 [hep-ph].
- [9] M. Kawasaki, K. Saikawa, and T. Sekiguchi, Axion dark matter from topological defects, *Phys. Rev. D* **91**, 065014 (2015), arXiv:1412.0789 [hep-ph].
- [10] E. Berkowitz, M. I. Buchoff, and E. Rinaldi, Lattice QCD input for axion cosmology, *Phys. Rev. D* **92**, 034507 (2015), arXiv:1505.07455 [hep-ph].
- [11] L. Fleury and G. D. Moore, Axion dark matter: strings and their cores, *JCAP* **01**, 004, arXiv:1509.00026 [hep-ph].
- [12] C. Bonati, M. D’Elia, M. Mariti, G. Martinelli, M. Mesiti, F. Negro, F. Sanfilippo, and G. Villadoro, Axion phenomenology and θ -dependence from $N_f = 2 + 1$ lattice QCD, *JHEP* **03**, 155, arXiv:1512.06746 [hep-lat].
- [13] P. Petreczky, H.-P. Schadler, and S. Sharma, The topological susceptibility in finite temperature QCD and axion cosmology, *Phys. Lett. B* **762**, 498 (2016), arXiv:1606.03145 [hep-lat].
- [14] G. Ballesteros, J. Redondo, A. Ringwald, and C. Tamarit, Unifying inflation with the axion, dark matter, baryogenesis and the seesaw mechanism, *Phys. Rev. Lett.* **118**, 071802 (2017), arXiv:1608.05414 [hep-ph].
- [15] V. B. . Klaer and G. D. Moore, The dark-matter axion mass, *JCAP* **11**, 049, arXiv:1708.07521 [hep-ph].
- [16] M. Buschmann, J. W. Foster, and B. R. Safdi, Early-Universe Simulations of the Cosmological Axion, *Phys. Rev. Lett.* **124**, 161103 (2020), arXiv:1906.00967 [astro-ph.CO].
- [17] M. Gorghetto, E. Hardy, and G. Villadoro, More axions from strings, *SciPost Phys.* **10**, 050 (2021), arXiv:2007.04990 [hep-ph].
- [18] M. Buschmann, J. W. Foster, A. Hook, A. Peterson, D. E. Willcox, W. Zhang, and B. R. Safdi, Dark Matter from Axion Strings with Adaptive Mesh Refinement, (2021), arXiv:2108.05368 [hep-ph].
- [19] P. Sikivie and Q. Yang, Bose-einstein condensation of dark matter axions, *Phys. Rev. Lett.*

103, 111301 (2009).

[20] P. Sikivie, The emerging case for axion dark matter, *Physics Letters B* **695**, 22 (2011).

[21] N. Banik and P. Sikivie, Axions and the galactic angular momentum distribution, *Phys. Rev. D* **88**, 123517 (2013).

[22] J. E. Kim, Weak Interaction Singlet and Strong CP Invariance, *Phys. Rev. Lett.* **43**, 103 (1979).

[23] M. A. Shifman, A. I. Vainshtein, and V. I. Zakharov, Can Confinement Ensure Natural CP Invariance of Strong Interactions?, *Nucl. Phys. B* **166**, 493 (1980).

[24] M. Dine, W. Fischler, and M. Srednicki, A Simple Solution to the Strong CP Problem with a Harmless Axion, *Phys. Lett. B* **104**, 199 (1981).

[25] A. R. Zhitnitsky, On Possible Suppression of the Axion Hadron Interactions. (In Russian), *Sov. J. Nucl. Phys.* **31**, 260 (1980).

[26] P. Sikivie, Experimental tests of the "invisible" axion, *Phys. Rev. Lett.* **51**, 1415 (1983).

[27] P. Sikivie, Detection rates for "invisible"-axion searches, *Phys. Rev. D* **32**, 2988 (1985).

[28] C. Hagmann, D. Kinion, W. Stoeffl, K. van Bibber, E. Daw, H. Peng, L. J. Rosenberg, J. LaVeigne, P. Sikivie, N. S. Sullivan, D. B. Tanner, F. Nezrick, M. S. Turner, D. M. Moltz, J. Powell, and N. A. Golubev, Results from a high-sensitivity search for cosmic axions, *Phys. Rev. Lett.* **80**, 2043 (1998).

[29] S. J. Asztalos, E. Daw, H. Peng, L. J. Rosenberg, D. B. Yu, C. Hagmann, D. Kinion, W. Stoeffl, K. van Bibber, J. LaVeigne, P. Sikivie, N. S. Sullivan, D. B. Tanner, F. Nezrick, and D. M. Moltz, Experimental constraints on the axion dark matter halo density, *The Astrophysical Journal* **571**, L27 (2002).

[30] S. J. Asztalos, R. F. Bradley, L. Duffy, C. Hagmann, D. Kinion, D. M. Moltz, L. J. Rosenberg, P. Sikivie, W. Stoeffl, N. S. Sullivan, D. B. Tanner, K. van Bibber, and D. B. Yu, Improved rf cavity search for halo axions, *Phys. Rev. D* **69**, 011101 (2004).

[31] S. J. Asztalos, G. Carosi, C. Hagmann, D. Kinion, K. van Bibber, M. Hotz, L. J. Rosenberg, G. Rybka, J. Hoskins, J. Hwang, P. Sikivie, D. B. Tanner, R. Bradley, and J. Clarke, Squid-based microwave cavity search for dark-matter axions, *Phys. Rev. Lett.* **104**, 041301 (2010).

[32] N. Du, N. Force, R. Khatiwada, E. Lentz, R. Ottens, L. J. Rosenberg, G. Rybka, G. Carosi, N. Woollett, D. Bowring, A. S. Chou, A. Sonnenschein, W. Wester, C. Boutan, N. S. Oblath, R. Bradley, E. J. Daw, A. V. Dixit, J. Clarke, S. R. O'Kelley, N. Crisosto, J. R. Gleason, S. Jois,

- P. Sikivie, I. Stern, N. S. Sullivan, D. B. Tanner, and G. C. Hilton (ADMX Collaboration), Search for invisible axion dark matter with the axion dark matter experiment, Phys. Rev. Lett. **120**, 151301 (2018).
- [33] T. Braine, R. Cervantes, N. Crisosto, N. Du, S. Kimes, L. J. Rosenberg, G. Rybka, J. Yang, D. Bowring, A. S. Chou, R. Khatiwada, A. Sonnenschein, W. Wester, G. Carosi, N. Woollett, L. D. Duffy, R. Bradley, C. Boutan, M. Jones, B. H. LaRoque, N. S. Oblath, M. S. Taubman, J. Clarke, A. Dove, A. Eddins, S. R. O’Kelley, S. Nawaz, I. Siddiqi, N. Stevenson, A. Agrawal, A. V. Dixit, J. R. Gleason, S. Jois, P. Sikivie, J. A. Solomon, N. S. Sullivan, D. B. Tanner, E. Lentz, E. J. Daw, J. H. Buckley, P. M. Harrington, E. A. Henriksen, and K. W. Murch (ADMX Collaboration), Extended search for the invisible axion with the axion dark matter experiment, Phys. Rev. Lett. **124**, 101303 (2020).
- [34] A. Collaboration, C. Bartram, T. Braine, E. Burns, R. Cervantes, N. Crisosto, N. Du, H. Korandla, G. Leum, P. Mohapatra, T. Nitta, L. J. Rosenberg, G. Rybka, J. Yang, J. Clarke, I. Siddiqi, A. Agrawal, A. V. Dixit, M. H. Awida, A. S. Chou, M. Hollister, S. Knirck, A. Sonnenschein, W. Wester, J. R. Gleason, A. T. Hipp, S. Jois, P. Sikivie, N. S. Sullivan, D. B. Tanner, E. Lentz, R. Khatiwada, G. Carosi, N. Robertson, N. Woollett, L. D. Duffy, C. Boutan, M. Jones, B. H. LaRoque, N. S. Oblath, M. S. Taubman, E. J. Daw, M. G. Perry, J. H. Buckley, C. Gaikwad, J. Hoffman, K. W. Murch, M. Goryachev, B. T. McAllister, A. Quiskamp, C. Thomson, and M. E. Tobar, Search for ”invisible” axion dark matter in the 3.3-4.2 μeV mass range (2021), arXiv:2110.06096 [hep-ex].
- [35] K. M. Backes, D. A. Palken, S. A. Kenany, B. M. Brubaker, S. B. Cahn, A. Droster, G. C. Hilton, S. Ghosh, H. Jackson, S. K. Lamoreaux, and et al., A quantum enhanced search for dark matter axions, Nature **590**, 238–242 (2021).
- [36] O. Kwon, D. Lee, W. Chung, D. Ahn, H. Byun, F. Caspers, H. Choi, J. Choi, Y. Chong, H. Jeong, J. Jeong, J. E. Kim, J. Kim, i. m. c. b. u. Kutlu, J. Lee, M. Lee, S. Lee, A. Matlashov, S. Oh, S. Park, S. Uchaikin, S. Youn, and Y. K. Semertzidis, First results from an axion haloscope at capp around 10.7 μeV , Phys. Rev. Lett. **126**, 191802 (2021).
- [37] M. S. Turner, Periodic signatures for the detection of cosmic axions, Phys. Rev. D **42**, 3572 (1990).
- [38] M. Lisanti, Lectures on Dark Matter Physics, in *Theoretical Advanced Study Institute in Elementary Particle Physics: New Frontiers in Fields and Strings* (2017) pp. 399–446,

arXiv:1603.03797 [hep-ph].

- [39] J. Diemand, M. Kuhlen, P. Madau, M. Zemp, B. Moore, D. Potter, and J. Stadel, Clumps and streams in the local dark matter distribution, *Nature* **454**, 735 (2008), arXiv:0805.1244 [astro-ph].
- [40] V. Springel, J. Wang, M. Vogelsberger, A. Ludlow, A. Jenkins, A. Helmi, J. F. Navarro, C. S. Frenk, and S. D. M. White, The Aquarius Project: the subhalos of galactic halos, *Mon. Not. Roy. Astron. Soc.* **391**, 1685 (2008), arXiv:0809.0898 [astro-ph].
- [41] J. F. Navarro, C. S. Frenk, and S. D. M. White, The Structure of cold dark matter halos, *Astrophys. J.* **462**, 563 (1996), arXiv:astro-ph/9508025.
- [42] A. Burkert, The Structure of dark matter halos in dwarf galaxies, *Astrophys. J. Lett.* **447**, L25 (1995), arXiv:astro-ph/9504041.
- [43] G. R. Blumenthal, S. M. Faber, R. Flores, and J. R. Primack, Contraction of Dark Matter Galactic Halos Due to Baryonic Infall, *Astrophys. J.* **301**, 27 (1986).
- [44] O. Y. Gnedin, A. V. Kravtsov, A. A. Klypin, and D. Nagai, Response of dark matter halos to condensation of baryons: Cosmological simulations and improved adiabatic contraction model, *Astrophys. J.* **616**, 16 (2004), arXiv:astro-ph/0406247.
- [45] S. Mashchenko, J. Wadsley, and H. M. P. Couchman, Stellar Feedback in Dwarf Galaxy Formation, *Science* **319**, 174 (2008), arXiv:0711.4803 [astro-ph].
- [46] F. Governato *et al.*, At the heart of the matter: the origin of bulgeless dwarf galaxies and Dark Matter cores, *Nature* **463**, 203 (2010), arXiv:0911.2237 [astro-ph.CO].